

# Takens-Bogdanov bifurcation of travelling wave solutions in pipe flow

F. MELLIBOVSKY<sup>1</sup> AND B. ECKHARDT<sup>2</sup>

<sup>1</sup>Departament de Física Aplicada, Universitat Politècnica de Catalunya, 08034, Barcelona, Spain

<sup>2</sup>Fachbereich Physik, Philipps-Universität Marburg, D-35032 Marburg, Germany

(Received ?? and in revised form ??)

The appearance of travelling-wave-type solutions in pipe Poiseuille flow that are disconnected from the basic parabolic profile is numerically studied in detail. We focus on solutions in the 2-fold azimuthally-periodic subspace because of their special stability properties, but relate our findings to other solutions as well. Using time-stepping, an adapted *Krylov*-Newton method and Arnoldi iteration for the computation and stability analysis of relative equilibria, and a robust pseudo-arclength continuation scheme we unfold a double-zero (Takens-Bogdanov) bifurcating scenario as a function of Reynolds number ( $Re$ ) and wavenumber ( $\kappa$ ). This scenario is extended, by the inclusion of higher order terms in the normal form, to account for the appearance of supercritical modulated waves emanating from the upper branch of solutions at a degenerate Hopf bifurcation. These waves are expected to disappear in saddle-loop bifurcations upon collision with lower-branch solutions, thereby leaving stable upper-branch solutions whose subsequent secondary bifurcations could contribute to the formation of the phase space structures that are required for turbulent dynamics at higher  $Re$ .

## 1. Introduction

Subcritical transition and the sustainment of turbulence at moderate flow rates in shear flows is a problem of great theoretical complexity and practical relevance (Grossmann 2000; Eckhardt *et al.* 2007; Eckhardt 2009). Since Osbourne Reynolds (1883) much celebrated work on the onset of turbulent motion in a straight pipe of circular cross-section, this problem has become a benchmark of transition without linear instability, i.e. subcritical transition. Many theoretical (Boberg & Brosa 1988; Brosa & Grossmann 1999), numerical (Schmid & Henningson 1994; Zikanov 1996; Shan *et al.* 1999) and experimental (Wygnanski & Champagne 1973; Wygnanski *et al.* 1975; Darbyshire & Mullin 1995; Hof *et al.* 2006) efforts have been devoted at comprehending how the laminar state (Hagen-Poiseuille flow) becomes unstable to finite amplitude perturbations despite its linear stability (Pfenniger 1961; Meseguer & Trefethen 2003).

The numerical computation of finite amplitude secondary solutions in the form of travelling waves (Faisst & Eckhardt 2003; Wedin & Kerswell 2004), whose existence relies on a mechanism called the self-sustained process (Waleffe 1997), initially advanced to account for turbulent regeneration, has brought renewed interest to the problem within the dynamical systems community. These waves typically appear in saddle-node bifurcations and break some of the symmetries of the problem while retaining others (Pringle & Kerswell 2007; Pringle, Duguet & Kerswell 2009). Their lower branches have been repeatedly shown to dwell on the critical threshold (Duguet, Willis & Kerswell 2008; Mellibovsky & Meseguer 2009) separating the basins of attraction of laminar and turbulent flows, which suggests their implication in the transition process. Upper-branch

solutions, with wall frictions closer to turbulence, seem to play a role in developed turbulence (Schneider, Eckhardt & Vollmer 2007; Kerswell & Tutty 2007) and have been observed in experiments (Hof *et al.* 2004).

The 2-fold discrete azimuthally-periodic subspace constitutes a special case in that it contains a family of travelling waves with unusually low-dimensional unstable manifolds. All other known families of travelling waves exhibit at least one unstable mode within their subspace that is shared by all waves, thereby rendering the family globally unstable. This is not the case of a specific shift-reflect, 2-fold azimuthally-periodic family of travelling waves, the special stability properties of which can be qualified as *convenient*. Lower-branch solutions of this family possess a single unstable direction within the subspace, which ultimately assists bare symmetry-restricted time evolution in converging them numerically (Duguet, Willis & Kerswell 2008), when adequately combined with edge tracking techniques (Skufca, Yorke & Eckhardt 2006; Schneider, Eckhardt & Yorke 2007). The lower branch being a saddle, it would not be surprising if the upper branch constituted a stable node, at least for some of the parameter values. Additional unstable directions arise when analysing the stability in full space or when considering subharmonic instability to longer wavelengths, but the convenient stability properties within their azimuthal subspace, which can by itself sustain turbulence, renders it a particularly nice playground for the search of all sorts of time-dependent solutions with simple numerical machinery. These solutions may help understand turbulence within the subspace and give hints as to what might be happening in full space.

This study aims at analysing and describing the phenomena associated to the emergence of disconnected solutions in shear flows. While the current analysis focuses on a given family of travelling waves in circular pipe flow, the results are thought to be common feature in a vast range of other travelling wave families in pipe flow and several equilibria and relative equilibria in a variety of other shear flows such as plane Couette (Nagata 1997; Wang, Gibson & Waleffe 2007) or plane Poiseuille (Pugh & Saffman 1988; Soibelman & Meiron 1991; Ehrenstein & Koch 1991) flows.

The outline of the paper is as follows. In §2, we present the pipe Poiseuille flow problem and sketch a numerical scheme for the integration of the resulting equations. The symmetries of the problem are discussed and numerical methods for the computation and stability analysis of relative equilibria are introduced. Some aspects of normal form reduction in the case of bifurcating relative equilibria are also reviewed in §2. The main results of the computations are presented in §3, where the different types of solutions resulting from an extensive parameter space exploration are exhibited, and evidence of a double-zero bifurcation scenario is exposed. These results are thoroughly discussed and explained in §4 by considering the inclusion of higher order terms in the relevant normal form. Conclusions and ensuing prospects and challenges are summarised in §5.

## 2. Formulation and methods

### 2.1. Equations and numerical scheme

The constant flow-rate motion of an incompressible Newtonian fluid through a straight pipe of circular cross-section is considered. The governing parameter is the Reynolds number, defined as  $Re = UD/\nu$ , where  $U$  is the mean axial flow speed,  $D$  the pipe diameter and  $\nu$  the kinematic viscosity of the fluid. The dynamics is governed by the incompressible Navier-Stokes equations.

In cylindrical nondimensional coordinates  $\mathbf{x} = (r, \theta, z)$ , the basic Hagen-Poiseuille solution of the Navier-Stokes problem reads  $\mathbf{u}_b = u_r^b \hat{\mathbf{r}} + u_\theta^b \hat{\boldsymbol{\theta}} + u_z^b \hat{\mathbf{z}} = (1 - r^2) \hat{\mathbf{z}}$ . The

Navier-Stokes equations for the velocity-pressure  $\mathbf{u} = (u_r, u_\theta, u_z)$ - $p$  perturbation fields are

$$\partial_t \mathbf{u} = -\nabla p + \frac{1}{Re} \Delta \mathbf{u} - (\mathbf{u} \cdot \nabla)(\mathbf{u}_b + \mathbf{u}) - (\mathbf{u}_b \cdot \nabla) \mathbf{u} + f \hat{\mathbf{z}}, \quad (2.1)$$

$$\nabla \cdot \mathbf{u} = 0, \quad (2.2)$$

$$Q(\mathbf{u}) = \int_0^{2\pi} \int_0^1 (\mathbf{u} \cdot \hat{\mathbf{z}}) r dr d\theta = 0, \quad (2.3)$$

$$\mathbf{u}(1, \theta, z; t) = \mathbf{0}, \quad \mathbf{u}(r, \theta + 2\pi/n_s, z, t) = \mathbf{u}(r, \theta, z + 2\pi/\kappa, t) = \mathbf{u}(r, \theta, z, t), \quad (2.4)$$

where an adjustable axial forcing  $f = f(t)$  in (2.1) ensures the constant mass-flux constraint (2.3). The non-slip boundary condition at the wall and the axial and azimuthal periodicities are enforced by (2.4), where  $\kappa$  is the non-dimensional wavenumber, here considered as an additional parameter selecting the axial periodicity of the flow structures. In this study, the axial wavenumber is varied in the range  $\kappa \in [1.1, 1.85]$ , corresponding to pipe periodicities  $\Lambda \in [3.40, 5.71]$ , in units of  $D/2$ . This range covers all relevant existing solutions up to  $Re \simeq 1500$  while discarding subharmonic instabilities that might complicate the bifurcation scenario under examination at higher  $Re$ . The azimuthal wavenumber is set to  $n_s = 2$  throughout, meaning that only 2-fold azimuthally-periodic fields are considered. All solutions living in this subspace are also solutions to the full Navier-Stokes equations with  $n_s = 1$ , but the instabilities associated to perturbations without the  $n_s = 2$  symmetry are suppressed, rendering some of the solutions stable and thus accessible through time evolution.

For the spatial discretisation of (2.1-2.4) we use a solenoidal spectral Petrov-Galerkin scheme thoroughly described and tested by Meseguer & Mellibovsky (2007). The method implicitly fulfils divergence free and boundary conditions, and dispenses with the need for dealing with the pressure field. The velocity field is expanded following

$$\mathbf{u}(r, \theta, z; t) = \sum_{l=-L}^L \sum_{n=-N}^N e^{-i(\kappa l z + n_s n \theta)} \mathbf{u}_{ln}(r; t), \quad (2.5)$$

$$\mathbf{u}_{ln}(r; t) = \sum_{m=0}^M a_{lnm}^{(1,2)}(t) \mathbf{v}_{lnm}^{(1,2)}(r), \quad (2.6)$$

with  $a_{lnm}^{(1,2)}$  the complex expansion coefficients defining the vector state  $\mathbf{a}$ . In this way, the field decouples into its axial-azimuthal Fourier components  $\mathbf{u}_{ln}$ . As already noted, the expansion basis  $\mathbf{v}_{lnm}(r)$ , presented in the work of Meseguer & Mellibovsky (2007, eq. (24-27)), is chosen so that boundary conditions (2.4) and solenoidality (2.2) are implicitly satisfied. The spectral resolution, checked as adequate for the computations performed in this study, has been set to  $L = 16$ ,  $N = 12$  and  $M = 36$ , corresponding to  $\pm 16$  axial and  $\pm 24$  azimuthal Fourier modes, and to 37 Chebyshev collocation points for the radial coordinate. Upon projection on the test basis  $\tilde{\mathbf{v}}_{lnm}(r)$  (Meseguer & Mellibovsky 2007, eq. (32-35)), we are left with a system of ordinary differential equations for the complex-valued state vector  $\mathbf{a}$ :

$$A \dot{\mathbf{a}} = \left( \frac{1}{Re} B_1 + B_2 \right) \mathbf{a} - \mathbf{b}(\mathbf{a}, \mathbf{a}) + f \mathbf{C}, \quad (2.7)$$

$$\mathbf{Q} \cdot \mathbf{a} = 0, \quad (2.8)$$

where the subscripts in Meseguer & Mellibovsky (2007, eq. (47)) have been omitted for simplicity and  $B$  has been decomposed into two separate contributions,  $B_1$  corresponding

to the viscous dissipation term, with the dependence on  $Re$  rendered explicit, and  $B_2$  to the linear advection terms.  $\mathbf{C}$  is the projection of  $\hat{\mathbf{z}}$  onto the test basis and is therefore responsible for keeping the mass-flux constant, represented by the linear scalar equation (2.8), by instantaneous adjustment of  $f$ .

The system (2.7) is evolved in time using a 4th order linearly implicit method with  $\Delta t = 1 \times 10^{-2}$ , where time is measured in units of  $D/(4U)$ .

It will be handy to define some global properties of the flow that are independent of solid-body motions such as translation or rotation. One such quantity is the normalised energy of any given perturbation field  $\mathbf{u}$ , which is given by

$$\varepsilon(\mathbf{u}) = \frac{1}{2\epsilon_b} \int_0^{2\pi/\kappa} dz \int_0^{2\pi} d\theta \int_0^1 r dr \mathbf{u}^* \cdot \mathbf{u}, \quad (2.9)$$

with  $\epsilon_b = \pi^2/(3\kappa)$  the energy of the basic flow and  $*$  symbolising complex conjugation. This energy decouples exactly into the sum of its axial-azimuthal Fourier components:

$$\varepsilon(\mathbf{u}) = \sum_{l=-L}^L \sum_{n=-N}^N \varepsilon_{ln} = \varepsilon_{1D} + \varepsilon_{2t} + \varepsilon_{2z} + \varepsilon_{3D}, \quad (2.10)$$

where  $\varepsilon_{ln} = \varepsilon(\mathbf{u}_{ln})$  is the energy associated to the  $(l, n)$  axial-azimuthal Fourier mode. To the right of (2.10) the Fourier modes have been grouped in meaningful sets corresponding to the axisymmetric streamwise-independent component ( $\varepsilon_{1D}$ , mean flow component), the non-axisymmetric streamwise-independent component ( $\varepsilon_{2z}$ , energy signature of vortices and streaks), the axisymmetric streamwise-dependent component ( $\varepsilon_{2\theta}$ , mean wavy component) and the non-axisymmetric streamwise-dependent component ( $\varepsilon_{3D}$ , purely three-dimensional energy).

Another global property is the mean axial pressure gradient that is required to drive the flow at constant mass-flux, relative to its laminar flow value. It can be easily stated in terms of the adjusting intensity of the axial forcing  $f$  and of  $Re$ :

$$(\nabla p)_z = 1 + \frac{Re f}{4}. \quad (2.11)$$

Finally, it will be useful to define the instantaneous axial and azimuthal phase speeds for any given velocity field. Their definition is clear for solid-body moving solutions, but can be extended to any velocity field by decomposing the time-evolving state vector into two contributions: one associated to solid-body motion and the other to a modulation. This decomposition can be made unique by minimising, as a function of the phase speeds, at any given time, the 2-norm of the modulational component:

$$\min_{c_z, c_\theta} \left\| a(t + \Delta t) - a(t) e^{-i(\kappa l c_z + n_s n c_\theta) \Delta t} \right\| \quad (2.12)$$

For all rotating and travelling waves,  $c_z$  and  $c_\theta$  are constant, the minimum (2.12) is exactly zero, and they coincide with the axial and azimuthal phase speeds, respectively. The effective computation is done instantaneously by considering two consecutive time instants separated by  $\Delta t$  and by applying a root-finding Newton method to the 2-dimensional Jacobian of the norm in (2.12).

## 2.2. Symmetries of the problem

Pipe flow and its basic solution possess  $O(2) \times SO(2)$  symmetry, i.e. it is invariant under all azimuthal rotations about the axis and reflections with respect to all diametral planes, as well as under all axial translations. All travelling wave families discovered so far are periodic and have axial and azimuthal dependency, thus breaking all continuous symmetries.

While, in the azimuthal direction, the natural periodicity of the pipe renders all solutions invariant under rotations of  $2\pi$ , travelling waves can have an additional discrete symmetry that renders them invariant under the cyclic group  $Z_{n_s} = \{R_{2\pi}, R_{2\pi/2}, \dots, R_{2\pi/n_s}\}$  with  $n_s$  the azimuthal wave number and

$$R_\alpha(\mathbf{u})(\mathbf{x}) = R_\alpha(u, v, w)(r, \theta, z; t) = (u, v, w)(r, \theta + \alpha, z; t). \quad (2.13)$$

In the axial direction, on top of the trivial shift by a wavelength, the axial symmetry rupture gives rise to a special type of time periodicity, in the sense that the time dependence is a bare drift in the direction of the  $SO(2)$  symmetry. Travelling waves are therefore best described as relative equilibria that possess the continuous space-time symmetry

$$(u, v, w)_{\text{tw}}(r, \theta, z; t) = (u, v, w)_{\text{tw}}(r, \theta, z - c_z t; 0), \quad (2.14)$$

where  $c_z$  is the axial drift speed. In a comoving reference frame travelling downstream with speed  $c_z$ , travelling waves appear as stationary solutions. Near a relative equilibrium the drift dynamics is trivial and decouples from the dynamics orthogonal to the drift. As a result, bifurcations of relative equilibria can be analysed in two steps, first describing the bifurcations associated to the orthogonal dynamics, then adding the corresponding drift along the travelling direction (Krupa 1990).

There are a couple of additional non-trivial symmetries that leave some of the known travelling waves unaltered. The first one is a mirror symmetry with respect to  $n_s$  diametral planes:

$$M\mathbf{u}(\mathbf{x}) = M(u, v, w)(r, \theta_i + \theta, z; t) = (u, -v, w)(r, \theta_i - \theta, z; t), \quad (2.15)$$

with  $\theta_i = \theta_0 + i\pi/n_s$ ,  $i = \{0, 1, \dots, n_s - 1\}$ , and  $\theta_0$  parametrising the azimuthal degeneracy of solutions.

The second one, characteristic of the travelling wave family studied here, is a combined shift-reflect symmetry. Solutions invariant under this symmetry operation,

$$S\mathbf{u}(\mathbf{x}) = S(u, v, w)(r, \theta_i + \theta, z; t) = (u, -v, w)(r, \theta_i - \theta, z + \pi/\kappa; t), \quad (2.16)$$

are left unaltered when shifted half a wavelength downstream and then reflected with respect to any of  $n_s$  diametral planes tilted with  $\theta_i$ .

A number of highly symmetric solutions possessing both symmetries (Pringle *et al.* 2009) have been identified and continued to very low  $Re$  numbers. Some of the less symmetric waves are known to emerge from symmetry breaking bifurcations of these highly symmetric waves.

All symmetries can be enforced upon computation. This obviously applies to time evolution, computation of relative equilibria using Newton iteration and stability analysis of relative equilibria via Arnoldi iteration. Nevertheless, we have chosen to only restrict the azimuthal wave number  $n_s$ , apart from the invariance due to axial periodicity, to avoid inevitable instability to azimuthally non-symmetric flows. Every additional symmetry has been exposed to eventual break-up.

### 2.3. Computation of relative equilibria, continuation and stability analysis

The spectral method discussed in section 2.1 is extremely versatile and very well suited for straightforward coding of a Newton method for the computation of relative equilibria, for their continuation in parameter space and for linear stability analysis using Arnoldi iteration. Some of these usages of the spectral method were briefly described in Meseguer *et al.* (2007) but will be developed further here.

### 2.3.1. Computation of travelling/rotating waves

The spectral representation of a generic travelling and/or rotating wave reduces to

$$\mathbf{a}(t) = \mathbf{a}_{\text{tw}} e^{-i(\kappa l c_z + n_s n c_\theta)t}, \quad (2.17)$$

where  $\mathbf{a}_{\text{tw}}$  is the state vector corresponding to the time-independent structure of the wave and  $c_z$  and  $c_\theta$  are the axial and azimuthal advection speeds, respectively. The travelling-waves family studied here has no rotation and, therefore,  $c_\theta = 0$ .

Substitution of (2.17) into (2.7,2.8) yields a non-linear system of algebraic equations

$$\begin{cases} \mathbf{F}(\mathbf{a}_{\text{tw}}, c_z, c_\theta, f) = \mathbf{0} \\ \mathbf{Q} \cdot \mathbf{a}_{\text{tw}} = 0 \\ \phi_z(\mathbf{a}_{\text{tw}}) = \phi_z(\mathbf{a}^0) \\ \phi_\theta(\mathbf{a}_{\text{tw}}) = \phi_\theta(\mathbf{a}^0) \end{cases}, \quad (2.18)$$

where the last two scalar equations impose the phase on any two suitable coefficients so as to lift the translational and rotational degeneracy of the solution. The vector function  $\mathbf{F}$  is given by

$$\mathbf{F}(\mathbf{a}_{\text{tw}}, c_z, c_\theta, f) = \left( \frac{1}{Re} \mathbf{B}_1 + \mathbf{B}_2 + i(\kappa l c_z + n_s n c_\theta) \mathbf{A} \right) \mathbf{a}_{\text{tw}} - \mathbf{b}(\mathbf{a}_{\text{tw}}, \mathbf{a}_{\text{tw}}) + f \mathbf{C}. \quad (2.19)$$

System (2.18) can be solved via Newton iteration. At step  $k$ , the linear system to be solved takes the form

$$\begin{bmatrix} D_{\mathbf{a}} \mathbf{G}^k & D_{c_z} \mathbf{G}^k & D_{c_\theta} \mathbf{G}^k & Re \mathbf{B}_1^{-1} \mathbf{C} \\ \phi_z^T & 0 & 0 & 0 \\ \phi_\theta^T & 0 & 0 & 0 \\ \mathbf{Q}^T & 0 & 0 & 0 \end{bmatrix} \begin{pmatrix} \Delta \mathbf{a}^k \\ \Delta c_z^k \\ \Delta c_\theta^k \\ \Delta f^k \end{pmatrix} = - \begin{pmatrix} \mathbf{G}^k \\ 0 \\ 0 \\ 0 \end{pmatrix}, \quad (2.20)$$

where Stokes preconditioning (multiplication by  $Re \mathbf{B}_1^{-1}$  from the left) has been applied to the first row to assist convergence (Mamun & Tuckerman 1995). Accordingly,  $\mathbf{G}^k = Re \mathbf{B}_1^{-1} \mathbf{F}(\mathbf{a}^k, c_z^k, c_\theta^k, f^k)$ . The terms appearing on the first row of the left hand side correspond to the Jacobian of  $\mathbf{G}$ , noted  $D_x \mathbf{G}$ , evaluated at step  $k$ :

$$\begin{cases} D_{\mathbf{a}} \mathbf{G}^k = I + Re \mathbf{B}_1^{-1} \mathbf{B}_2 + i Re (\kappa l c_z^k + n_s n c_\theta^k) \mathbf{B}_1^{-1} \mathbf{A} - Re \mathbf{B}_1^{-1} D_{\mathbf{a}} \mathbf{b}(\mathbf{a}^k) \\ D_{c_z} \mathbf{G}^k = i \kappa l Re \mathbf{B}_1^{-1} \mathbf{A} \mathbf{a}^k \\ D_{c_\theta} \mathbf{G}^k = i n_s n Re \mathbf{B}_1^{-1} \mathbf{A} \mathbf{a}^k \end{cases}, \quad (2.21)$$

where  $D_{\mathbf{a}} \mathbf{b}(\mathbf{a}^k) \Delta \mathbf{a}^k$ , the linearised nonlinear term, is computed in physical space as  $(\Delta \mathbf{u}^k \cdot \nabla) \mathbf{u}_{\text{tw}}^k + (\mathbf{u}_{\text{tw}}^k \cdot \nabla) \Delta \mathbf{u}^k$  and then projected back to spectral space (Meseguer & Mellibovsky 2007). Arrays  $\phi_z$  and  $\phi_\theta$  correspond to the linearisation of the phase prescription of any two coefficients, as long as they are associated with basis elements that entrain axial and azimuthal structure, respectively. In the notation of Meseguer & Mellibovsky (2007), we have chosen to fix the phase of  $a_{100}^{(2)}$  and  $a_{010}^{(2)}$  to lift the axial and azimuthal degeneracies of the solutions, respectively. The incremental vector the Newton method requires solving for at each step is defined as  $\Delta x^k = x^{k+1} - x^k$  and provides the new guess for step  $k+1$ .

The solution of the linear system at every Newton step needs only be approximated by using inexact Krylov iteration. Generalised minimal residuals (see Frayssé, Giraud, Gratton & Langou 2003, for the implementation of GMRES we use) and stabilised biconjugate gradient methods (BiCGSTab) can be easily implemented (see e.g. Quarteroni, Sacco & Saleri 2007, and references therein). Convergence to the exact solution of the nonlinear equations to numerical accuracy is guaranteed provided that a sufficiently good initial

guess  $(\mathbf{a}^0, c_z^0, c_\theta^0, f^0)$  is fed into the iteration. Convergence can be enhanced by appropriate damping (Quarteroni *et al.* 2007) or trust-region techniques (Dennis & Schnabel 1996).

### 2.3.2. Continuation of solutions

It is fairly easy to extend the Newton method just described to the continuation in  $Re$  of any branch of solutions. The explicit dependence of system (2.18) on  $Re$  allows this parameter to be treated as an additional unknown. Orthogonality to the Jacobian at some prescribed distance (pseudo-arclength) from the departing solution provides the additional equation needed (Sanchez, Marques & Lopez 2002). This continuation technique is capable of following branches around turning points, which makes it very convenient in the presence of saddle-node bifurcations. Continuation in the other parameter  $\kappa$  is not as straight forward. The complex dependency of the linear contribution of  $\mathbf{F}$  on  $\kappa$  requires recomputing the linear operators at every single Krylov iteration, which renders the method very costly. We have chosen to continue it manually by simply using the Newton method with discrete jumps in  $\kappa$ , small enough so that the converged solution at the previous  $\kappa$  constitutes a sufficiently good guess. This procedure cannot go around turning points, but combined with pseudo-arclength continuation in  $Re$ , the full family of travelling waves can be computed.

### 2.3.3. Stability analysis

Special care must be taken when analysing the linear stability of rotating/travelling waves. Waves of this type have two equivalent representations in the constant pressure gradient and in the constant flow-rate frames. This is so because their solid-body motion neither modifies the mass-flux nor the mean axial pressure gradient. However, their destabilisation does not necessarily preserve these two global quantities simultaneously, meaning that linear stability will explicitly depend on which of the two is prescribed as constant. Since we have chosen to study pipe flow at a constant flow rate, we must accordingly allow for pressure variation. Let us consider an infinitesimal perturbation  $(\mathbf{v}_a, v_f)$  on a given travelling/rotating wave  $(\mathbf{a}_{tw}, f_{tw})$  in a reference frame moving with the wave:

$$\begin{cases} \mathbf{a} = (\mathbf{a}_{tw} + \mathbf{v}_a e^{\lambda t}) e^{-i(\kappa l c_z + n_s n c_\theta)t} \\ f = f_{tw} + v_f e^{\lambda t} \end{cases} . \quad (2.22)$$

The factor  $e^{\lambda t}$  is intended to capture the linear evolution of the perturbation in the vicinity of the relative equilibrium. In this sense,  $(\mathbf{v}_a, v_f)$  is an eigenvector of eigenvalue  $\lambda$ , which in general can be complex. Introducing (2.22) into (2.7,2.8) yields the evolution equation for the perturbation, which can be linearised around the wave solution by discarding all second order terms:

$$\begin{cases} \left( \frac{1}{Re} B_1 + B_2 + i(\kappa l c_z + n_s n c_\theta) A - D_a \mathbf{b}(\mathbf{a}_{tw}) \right) \mathbf{v}_a + \mathbf{C} v_f = \lambda A \mathbf{v}_a \\ \mathbf{Q} \cdot \mathbf{v}_a = 0 \end{cases} . \quad (2.23)$$

System (2.23) constitutes a constrained generalised eigenproblem which can be expressed in matrix form as

$$\mathcal{A} \mathbf{x} = \lambda \mathcal{M} \mathbf{x}, \quad (2.24)$$

where

$$\begin{aligned} \mathcal{A} &= \begin{bmatrix} \frac{1}{Re} B_1 + B_2 + i(\kappa l c_z + n_s n c_\theta) A - D_a \mathbf{b}(\mathbf{a}_{tw}) & \mathbf{C} \\ \mathbf{Q}^T & 0 \end{bmatrix}, \\ \mathcal{M} &= \begin{bmatrix} A & \mathbf{0} \\ \mathbf{0}^T & 0 \end{bmatrix} \quad \text{and} \quad \mathbf{x} = \begin{pmatrix} \mathbf{v}_a \\ v_f \end{pmatrix}. \end{aligned} \quad (2.25)$$

Since we are only interested in leading eigenvalues (those with larger real part) while usual iterative methods are good at capturing dominant eigenvalues (those with larger modulus), we solve (2.24) in shift-invert mode:

$$(\mathcal{A} - \sigma \mathcal{M})^{-1} \mathcal{M} \mathbf{x} = \nu \mathbf{x}, \quad \nu = \frac{1}{\lambda - \sigma}, \quad (2.26)$$

with a real shift  $\sigma$  applied to avoid the neutrally stable double eigenvalue at the origin corresponding to infinitesimal rotations and translations.

The method used is Arnoldi iteration with Krylov-based iteration for the solution of the linear system involved at each step (Freitag 2007). We use the robust routines by Lehoucq & Scott (1996). Stokes preconditioning is employed as for the Newton method to speed up convergence.

#### 2.4. Normal form reduction

We will be concerned here with the stability and bifurcation of travelling-wave-type solutions. Strictly speaking, a Poincaré section should be defined and the bifurcation analysis carried out for the map defined by the resulting Poincaré application. In this setting, travelling waves would be seen as fixed points and modulated waves as periodic orbits. It is common practice, though, to approximate the map to any desired accuracy with a system of differential equations (see Guckenheimer & Holmes 1983, chapter 4). Bifurcations of maps can thus be studied by constructing continuous-time normal forms. This comes out naturally when studying the stability of relative equilibria in a comoving reference frame (2.22). In the close neighbourhood of the relative (or degenerate) equilibrium, such an analysis is perfectly accurate (Rand 1982; Krupa 1990). These travelling waves may typically undergo Hopf bifurcations. The bifurcation is considered a Hopf bifurcation from a relative equilibrium rather than a Neimark-Sacker (Hopf bifurcation for maps) because of the special type of time-dependence involved. The bifurcating quasi-periodic solution is a modulated travelling wave which is just a periodic orbit in the comoving frame in which the travelling wave is stationary. Modulated waves that bifurcate via Hopf bifurcations from drifting waves in systems with  $SO(2)$  symmetry were classified in terms of the spatial symmetry of the drifting wave by Rand (1982). The classification was completed by Golubitsky, LeBlanc & Melbourne (2000) to include the spatiotemporal symmetry of the modulated wave. The appropriate way to investigate these solutions is to study the dynamics normal to the group orbit (Krupa 1990), which in our case is equivalent to considering the dynamics in a moving reference frame in which the travelling wave is stationary.

A problem arises when, for given values of the parameters, coexistence of several waves occurs and, possibly, of one or more modulated waves. In this case, each wave will generally drift with its own phase speed, so that there is no unique moving reference frame in which their degeneracy could be lifted simultaneously. This is easily overcome by stating the problem back with the use of Poincaré sections, combined with continuous-time interpolation of the corresponding maps. This of course only solves the problem as long as the limits of validity of the interpolation are not infringed. In particular, special care should be taken when studying the dynamics in the vicinity of homoclinic orbits, where arbitrarily small perturbations can lead to qualitatively different behaviour due to manifolds entanglement. In the absence of translational symmetry, complex dynamics would arise, i.e. horseshoes (Smale 1967; Guckenheimer & Holmes 1983). However, it is possible to show that, due to the translational symmetry of the pipe, if a point lies on both the stable and the unstable manifold of a saddle such as a lower-branch travelling wave, then



the unstable manifold is contained within the stable manifold and complex dynamics does not occur (Chossat & Lauterbach 2000).

It will be argued that, in the problem at hand, there are only two active modes in the range of parameters studied, all other modes being slaved to these two via the centre manifold theorem. This, added to the translational symmetry of the pipe, results in the ability of capturing the dynamics within this region of parameter space with a pair of amplitude equations:

$$\begin{cases} \dot{x} = F_1(x, y), \\ \dot{y} = F_2(x, y), \end{cases} \quad (2.27)$$

where  $x$  and  $y$  are real amplitudes related to velocity fields in (2.1). The simplest expansion for  $F_1$  and  $F_2$  that is compatible with the dynamics observed upon integration of (2.7) is the subject of normal form theory and will be developed along the analysis.

### 3. Results

#### 3.1. Travelling waves

The special stability properties of the specific family of travelling waves in the 2-fold periodic subspace singles them out for the kind of analysis performed in this study. These waves, whose existence relies on the *Self-Sustaining Process* (SSP) (Waleffe 1995, 1997), were first computed by Faisst & Eckhardt (2003) and Wedin & Kerswell (2004) using volume forcing homotopy. They are characterised by discrete 2-fold azimuthal periodicity ( $Z_2$ , i.e.  $n_s = 2$ ) and a combined shift-reflect symmetry ( $S$ ).

For a given  $\kappa$  and above a certain critical  $Re$ , they appear in pairs, one that is closer to the laminar solution, the other being further away in all respects and whatever the property examined (friction factor, energy contents, distance in phase space, etc). They are accordingly tagged as a lower-branch and an upper-branch solution, respectively. Figure 1 (see online movies) shows axial velocity contours together with in-plane velocity vectors on four cross-sections spanning half a wavelength for  $\kappa = 1.52$ ,  $Re = 1600$  upper-branch (top row) and lower-branch (bottom row) travelling waves. The discrete 2-fold azimuthal periodicity can be seen in all cross-sections. Also the combined shift-reflect symmetry can be grasped by comparing the  $z = 0$  and  $z = \Lambda/2$  cross-sections of either travelling wave. The reflection plane is tilted with  $\theta_0 \simeq \pi/4$ . The complementary half-wavelength is not shown, as it can be constructed by mere reflection of the given cross-sections. The travelling waves shown are representative of the full family in that they are characterised by wobbling low-speed streaks (light shading) in the pipe central region and fairly streamwise-independent high-speed streaks in the wall region (dark). Leaving aside weak secondary vortices, a couple of strong vortex pairs can be identified from the velocity vectors. In each of the pairs, the vortices are not of equal intensity, but alternate in strength along the axial direction. Except for the higher axial velocities and the slightly wider low speed streaks, not much distinguishes the upper-branch solution from the lower-branch solution.

Radial-velocity contour-lines on a radial plane at  $r = 0.65$  have been plotted in figure 2 for both travelling waves. The difference between upper-branch and lower-branch waves becomes clearer, the former involving much larger radial transport. These sections display clearly both the azimuthal periodicity and the shift-reflect symmetry of the waves. Structures resembling these and other travelling waves have been observed experimentally in developed turbulence (Hof *et al.* 2004) as well as in numerical simulation (Kerswell & Tutty 2007; Schneider, Eckhardt & Vollmer 2007; Willis & Kerswell 2008).

They appear in saddle-node bifurcations starting from  $Re \simeq 1358.5$  for the optimal

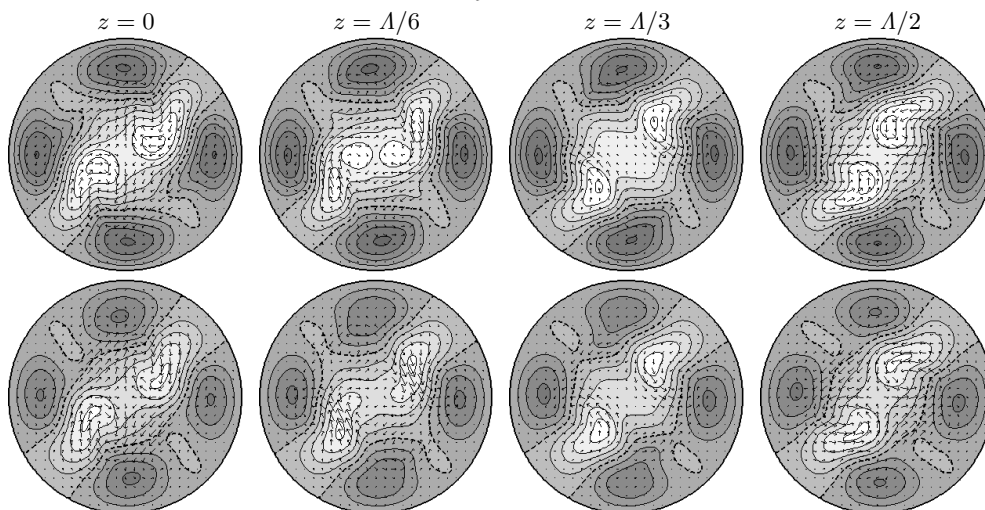


FIGURE 1. Cross-sections spanning half a wavelength ( $\Lambda/2 = \pi/\kappa$ ) of the upper-branch (top row) and the lower-branch (bottom row) travelling waves for  $\kappa = 1.52$ ,  $Re = 1600$ . Axial perturbation velocity contour-lines are equispaced with intervals of  $\Delta u_z = 0.1U$ . Regions where the axial velocity is faster or slower than the laminar parabolic profile are coded in dark and light, respectively, with the zero contour-line marked with a dashed line. In-plane velocity vectors are also shown.

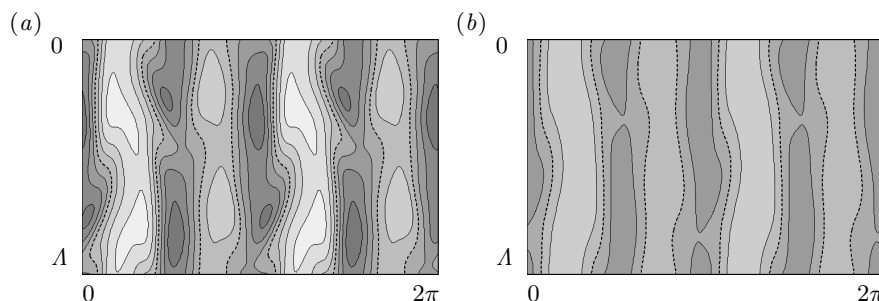


FIGURE 2. Radial sections at  $r = 0.65$  of (a) the upper-branch and (b) the lower-branch travelling waves for  $\kappa = 1.52$ ,  $Re = 1600$ . Radial velocity contour-lines are equispaced with intervals of  $\Delta u_r = 0.0072U$ . Regions where the flow goes towards the walls or the pipe center are shaded dark and light, respectively.

wave number  $\kappa \simeq 1.55$  (Wedin & Kerswell 2004). Lower-branch solutions exhibit a single unstable eigenmode when considered in the azimuthal subspace where they live, which makes them accessible through time integration if appropriately combined with edge tracking techniques. In this sense, they are edge states (Schneider *et al.* 2007) of the 2-fold azimuthally-periodic pipe, and they constitute an example of non-uniqueness of the edge state, since they coexist as attractors within the critical threshold, and for some range of  $\kappa$  and  $Re$ , with another family of travelling waves that are both shift-reflect and mirror symmetric and that have also a single unstable direction (Duguet *et al.* 2008). The stable manifold of these waves separates, albeit only locally, initial conditions that decay uneventfully from others that undergo turbulent transients. For this reason, lower-branch solutions are believed to play a central role in the transition process.

As already pointed out, lower-branch solutions, when continued down in  $Re$ , merge with upper-branch solutions in a saddle-node-type bifurcation. Around the saddle-node

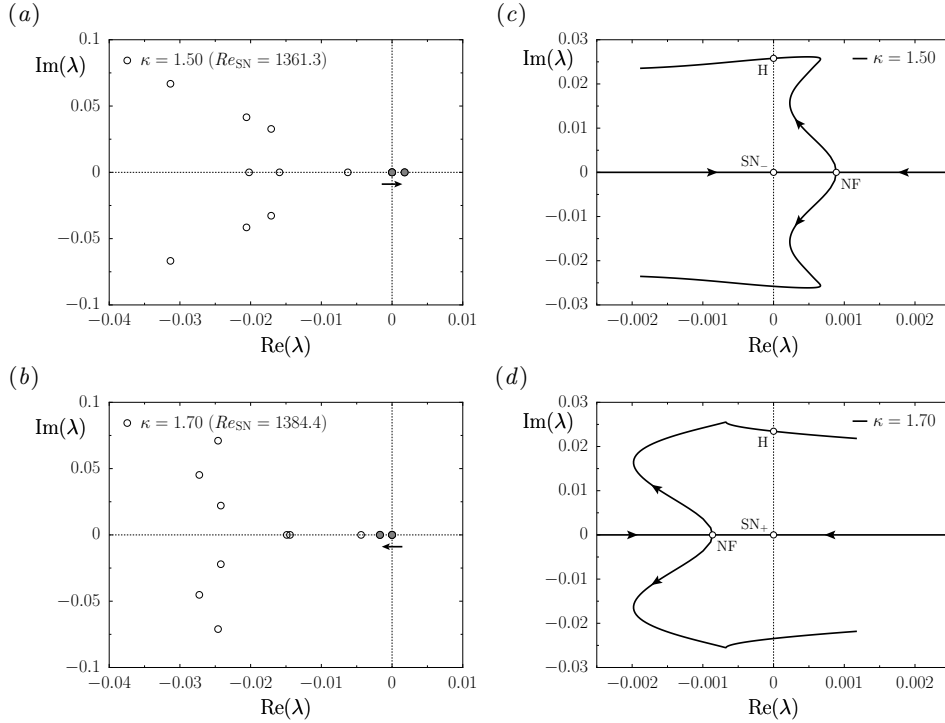


FIGURE 3. Rightmost eigenvalues of (a)  $\kappa = 1.50$  and (b)  $\kappa = 1.70$  travelling waves at their respective saddle-node bifurcation (SN). The direction of the zero-crossing from lower to upper branch is indicated with an arrow. The eigenvalues marked as filled circles have been followed across the saddle-node point and beyond for both (c)  $\kappa = 1.50$  and (d)  $\kappa = 1.70$ . Saddle-node (SN), node-focus (NF) and Hopf (H) points are identified with circles.

point, a real eigenvalue must cross the imaginary axis, either adding or subtracting an unstable direction. As a matter of fact, both scenarios occur and the stability properties of upper-branch solutions depend on the axial wavenumber  $\kappa$ . Upper-branch long waves are unstable, whilst short waves are stable. The spectrum of a long ( $\kappa = 1.50$ ) and of a short ( $\kappa = 1.70$ ) wave are shown in figures 3(a) and 3(b), respectively, at their respective saddle-node points. The arrow below the bifurcating eigenvalue points in the crossing direction when followed from lower to upper branch. For  $\kappa = 1.50$ , the solution goes from one to two unstable directions, while for  $\kappa = 1.70$  it goes from one to nil. Figures 3(c) and 3(d) show the trajectories followed by the two rightmost eigenvalues (filled circles in figures 3a,b) when continued across the saddle-node (SN) and beyond, for  $\kappa = 1.50$  and  $\kappa = 1.70$ , respectively. In both cases, the eigenvalues collide and go complex in a node-focus (NF) transition, but they can do so at either side of the imaginary axis. When followed further to higher  $Re$  along the upper branch, long and short solutions undergo a stabilising or destabilising Hopf bifurcation (H), respectively, implying the existence of modulated waves (relative periodic orbits).

Cross-sections of both travelling waves at their respective saddle-node points have been plotted in figures 4(a) and 4(c), together with their corresponding crossing eigenfunctions (figures 4b and 4d). It is clear from the contour plots that the effect of varying  $\kappa$  on the solutions does not affect the flow structure dramatically, aside from the stretching and the stability properties. It is also remarkable how the eigenfunctions corresponding to two different eigenvalues (figures 4c,d) look so similar to each other, even for different  $\kappa$ .

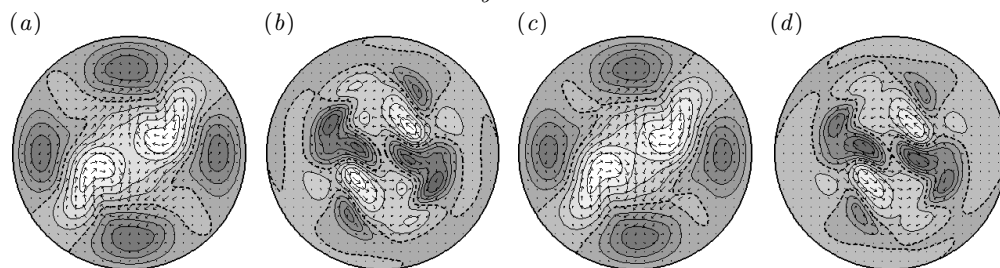


FIGURE 4. (a)  $\kappa = 1.50$  and (c)  $\kappa = 1.70$  travelling waves at their respective saddle-node bifurcation points (SN in figure 4). Also shown are the bifurcating eigenfunctions for (b)  $\kappa = 1.50$  and (d)  $\kappa = 1.70$ . Axial perturbation velocity contour-lines are equispaced in intervals of  $\Delta u_z = 0.1U$ .

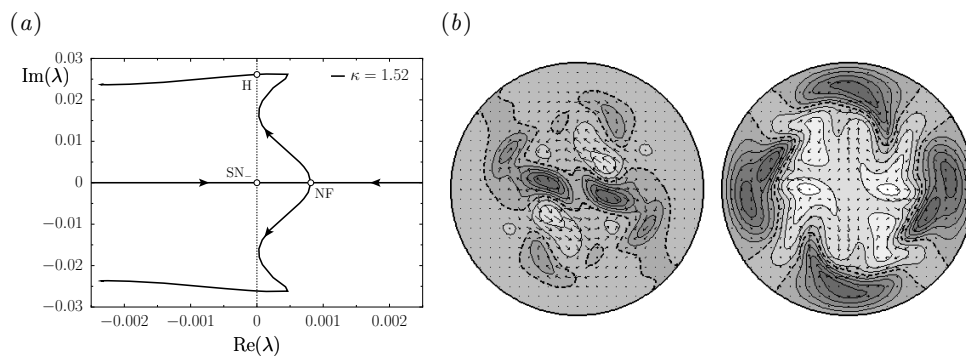


FIGURE 5. (a) Trajectories of the two rightmost eigenvalues for  $\kappa = 1.52$ . (b) Real (left) and imaginary (right) parts of the corresponding eigenvectors at the Hopf bifurcation (H,  $Re = 1775.4$ ).

This is a signature of the tendency to become parallel, which ultimately leads to collision in a node-focus (NF) transition. Both eigenfunctions preserve the same symmetries as the travelling waves, so that all solutions arising from their bifurcation must necessarily possess the same symmetries.

Wavenumber continuity suggests that there might be an intermediate value of  $\kappa$  for which the node-focus point can be brought to the origin of the complex plane. Appropriate tuning of  $\kappa$  and  $Re$  would therefore help unfold a codimension-two double zero bifurcation, a complete study of which is due to Takens (1974) and to Bogdanov (1975). As a matter of fact, the trajectories of the complex eigenvalues, following a left opening parabola plus an eventual right turn, indicate that for a certain range of  $\kappa$  an additional pair of crossings will take place, thus implying additional Hopf bifurcations closely related to the appearance of periodic orbits in a double-zero bifurcation.

### 3.2. Modulated travelling waves

Figure 5(a) depicts the trajectories of the relevant eigenvalues for  $\kappa = 1.52$ . They are extremely close to those observed for  $\kappa = 1.50$ , except that the nose is getting tangent to the imaginary axis. The implications of this will be discussed later on. Let us focus on the Hopf bifurcation (H) for the time being. The crossing takes place at  $Re = 1775.4$  on the upper branch, with the arrows pointing towards higher  $Re$ . The real and imaginary parts of the bifurcating eigenfunction are shown in figure 5(b) only for completeness, since it is difficult to extract from them relevant information on the nature of the instability

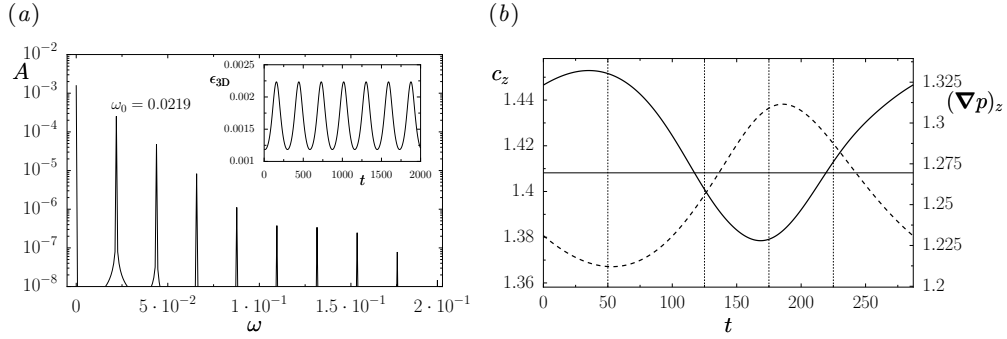


FIGURE 6. (a) Fourier transform of the non-axisymmetric streamwise-dependent modal energy contents ( $\varepsilon_{3D}$ ) time-stamp for the  $(\kappa, Re) = (1.52, 1600)$  modulated wave. The time signal is plotted in the inset. (b) Advection speed ( $c_z$ , solid line) and mean axial pressure gradient normalised by its laminar value ( $(\nabla p)_z$ , dashed line) along a full period. The values for the  $(\kappa, Re) = (1.52, 1600)$  upper-branch travelling wave are indicated by the horizontal line.

that they carry. As already noted, the instability does not break any of the symmetries exhibited by the bifurcating travelling wave.

The existence of a Hopf bifurcation implies the appearance of a time-periodic solution, in this case a modulated wave or relative periodic orbit. Since the crossing is leftwards as  $Re$  is increased, it necessarily carries with it a stabilisation of the upper-branch travelling wave, which was unstable at onset. The Hopf bifurcation happens to be supercritical in the sense that the first Lyapunov coefficient is negative (Kuznetsov 1995). This we infer from the fact that time evolution unveils a stable branch of modulated waves pointing towards decreasing  $Re$ .

Simple time evolution starting from the  $(\kappa, Re) = (1.52, 1600)$  unstable upper-branch travelling wave (figure 1, top row) departs in an oscillatory fashion, as predicted by the complex pair of unstable eigenvalues, to nonlinearly converge onto a modulated wave.

Travelling waves, which are degenerate or relative equilibria, and solutions bifurcating from them have a pure frequency associated to the advection speed (solid-body translation). Local quantities such as point velocities or pressures necessarily reflect on this frequency. However, since it reflects a neutral direction, it can be suppressed by restating the problem in a comoving frame. Global quantities such as modal energies or volume averaged fields naturally overlook solid-body rotation and translation, making them suitable for a decoupled analysis in the direction orthogonal to the degenerate drift. Thus, as justified before, the bifurcation analysis of travelling waves can be carried out analogously to that of fixed points, as long as special care is taken in the neighbourhood of homoclinic connections (Rand 1982; Golubitsky *et al.* 2000). The Hopf bifurcation adds a modulational frequency to the pure translational frequency. As a result, global quantities cease to be constant and oscillate with this frequency. The Fourier transform of the energy contained in non-axisymmetric streamwise-dependent modes ( $\varepsilon_{3D}$ ) has been plotted in figure 6(a), with the time signal shown in the inset frame. The spectrum reveals that the solution has a strong mean component and a peak angular frequency at  $\omega_0 = 0.0219$ , corresponding to a period  $T = 2\pi/\omega_0 = 286.7$ . This period is extremely long when compared with the streamwise advection time-scale, which is of order  $2\pi/(\kappa c_z) \sim 3$ . The signal is not strictly sinusoidal and some energy is spread among a number of harmonics of  $\omega_0$ . A full period of the axial advection speed ( $c_z$ ) and of the mean axial pressure gradient normalised by its laminar value ( $(\nabla p)_z$ ) has been plotted in figure 6(b). Both are global quantities and, as expected, oscillate with the modulational frequency  $\omega_0$ . The

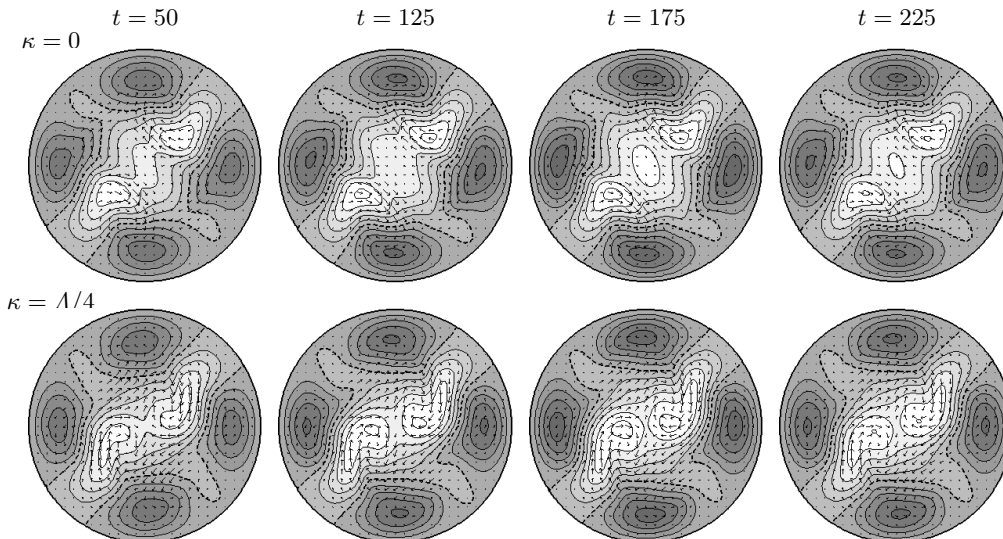


FIGURE 7. From left to right,  $t = 50, 125, 175$  and  $225$  snapshots of the  $((\kappa, Re) = (1.52, 1600))$  modulated wave, as indicated by the vertical dotted lines in figure 6(b). Shown are the  $z = 0$  (top row) and  $z = \Lambda/4$  (bottom row) cross-sections with axial velocity contour-lines equispaced in intervals of  $\Delta u_z = 0.1U$ . To avoid drift due to streamwise advection, snapshots are taken in a comoving frame travelling at the instantaneous advection speed from figure 6(b).

horizontal line indicates the constant value of these quantities for the unstable upper-branch travelling wave from which the modulated wave bifurcates. The modulated wave orbits in phase space around the travelling wave, so that the instantaneous values of the former oscillate around those of the latter. The differences between time-averaged quantities and travelling wave values are purely due to nonlinear effects, since for this  $Re$  and  $\kappa$  we are already some distance away from the linear influence of the instability.

Figure 7 (see online movie) depicts a couple of cross-sections ( $z = 0$ , top row;  $z = \Lambda/4$ , bottom row) of the modulated wave at four different time instants along one period (from left to right,  $t = 50, 125, 175$  and  $225$ ). The modulation is obvious from the series of snapshots yet not very prominent, as could be expected from the mild oscillation (within  $\pm 5\%$ ) of the time series in figure 6(b). Comparison with figure 1 (top row) reveals that the overall flow structure of the travelling wave is preserved on average but is now dependent on time.

Radial sections showing radial velocity contours have been plotted in figure 8 (see online movie) to convey in a clear way the modulation of the wave along a full period. It also confirms that all symmetries are preserved. It will soon become clear that the snapshot at  $t = 50$  is about the closest approach to the lower-branch travelling wave, while all of them are approximately equally distant from the upper-branch wave.

Straightforward  $Re$ -continuation of the  $\kappa = 1.52$  modulated waves by time evolution reveals that they bifurcate off the travelling waves upper branch precisely at the Hopf bifurcation point at  $Re = 1775.4$  (H in figure 5a). Figure 9 shows phase map representations of the modulated waves for a discrete set of  $Re$  along the branch. Two global quantities,  $\varepsilon_{3D}$  and  $(\nabla p)_z$ , have been chosen to get rid of axial drift effects. Increasing  $Re$  from  $Re = 1600$  (towards lighter gray), the modulated wave (solid closed loops) shrinks and closes on the upper-branch travelling wave (filled circles), to end up merging at the Hopf point ( $Re = 1775.4$ , not shown). In the opposite direction, the wave also starts shrinking but the process stops, slightly reverses and track of the wave is lost, as

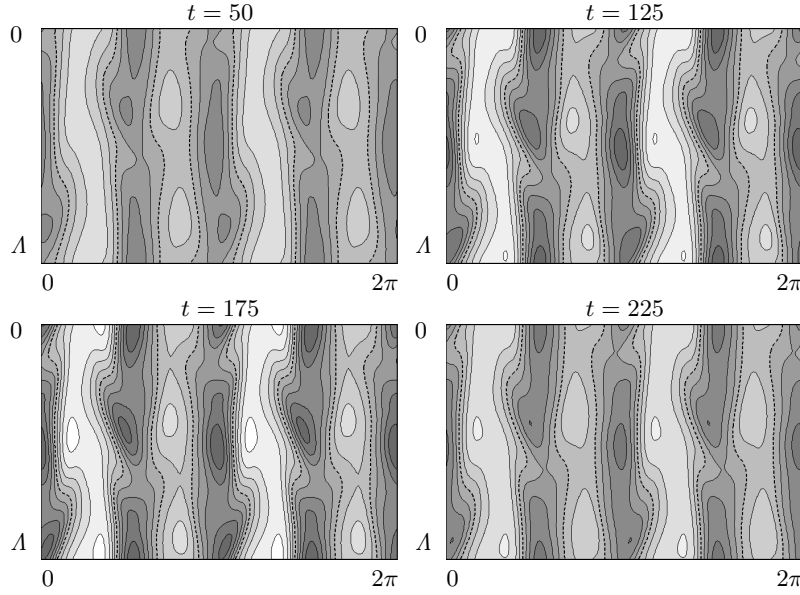


FIGURE 8. Radial sections at  $r = 0.65$  of the  $(\kappa, Re) = (1.52, 1600)$  modulated wave. Snapshots are taken in a reference frame moving at the wave speed. Radial velocity contour-lines are equispaced with intervals of  $\Delta u_r = 0.0072U$ . Regions where the flow goes towards the walls or the pipe center are shaded dark and light, respectively.

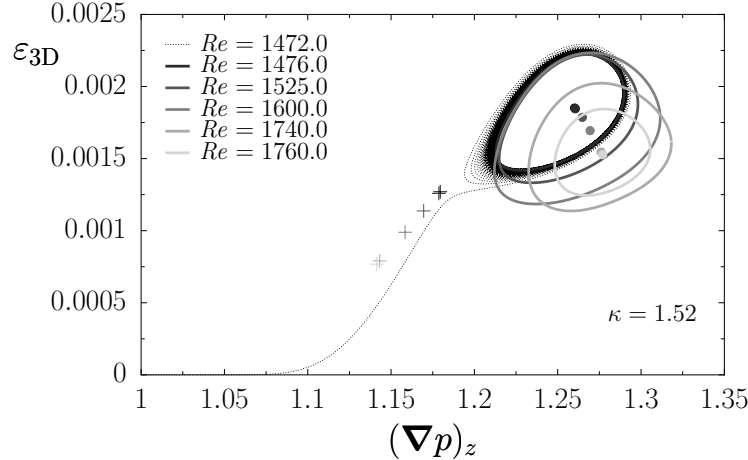


FIGURE 9. Phase map projections of travelling and modulated waves along a  $Re$ -continuation for  $\kappa = 1.52$ . The axes represent non-axisymmetric streamwise-dependent energy ( $\varepsilon_{3D}$ ) against mean axial pressure gradient ( $(\nabla p)_z$ ). Different gray intensities correspond to different  $Re$  as explained in the legend. Lower- and upper-branch travelling waves are marked with pluses and filled circles, respectively; modulated waves with solid lines and escaping trajectories with dotted lines.

pointed out by the diverging dotted trajectory. This trajectory wanders around a ghost of the disappeared modulated wave for some time, then spirals away until it comes close to the lower-branch travelling wave (plus signs) and leaves the region towards the laminar flow. Close analysis seems to indicate that the branch bends and turns around a fold (saddle-node) of cycles picking up an unstable direction. The phase map picture is, in this sense, incomplete. For each of the stable cycles (nodal branch) there must

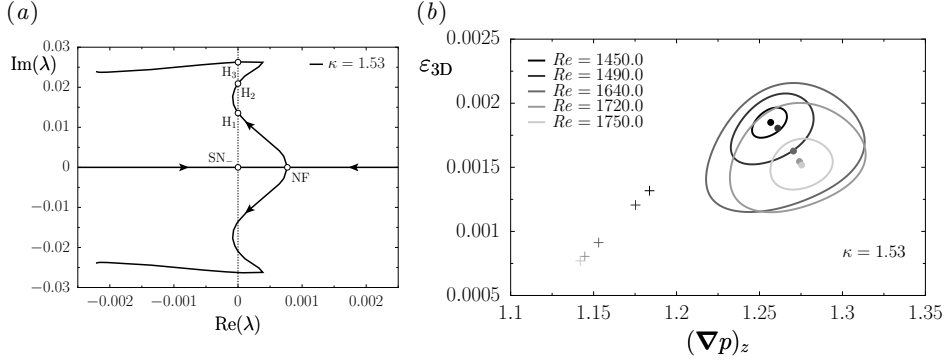


FIGURE 10. (a) Eigenvalues trajectories for  $\kappa = 1.53$ . (b) Phase map projections of travelling and modulated waves along a  $Re$ -continuation for  $\kappa = 1.53$ . See the caption of figure 9 for explanations.

be an unstable cycle (saddle branch). As  $Re$  increases from the fold-of-cycles point, the nodal branch approaches the upper branch of travelling waves until eventual collision at the Hopf point, while the saddle branch grows larger and larger. It will be argued later that, unless some exotic symmetry-breaking event takes place, the unstable modulated wave must end up colliding with the lower branch of travelling waves in a saddle-loop bifurcation, where it ceases to exist without any other consequence.

As already mentioned, decreasing  $Re$  causes both branches to merge in a fold-of-cycles, leaving unstable travelling waves as the only existing solutions. Any trajectory issued from the vicinity of the upper-branch wave spirals away, temporarily orbits around the ghost of the disappeared modulated wave, and then continues spiraling away until the trajectory manages to go around the lower-branch travelling wave and finally leaves towards the basic laminar profile  $(\varepsilon_{3D}, (\nabla p)_z) = (0, 1)$  along the only unstable direction of the travelling wave.

Continuation in the geometrical parameter  $\kappa$  causes the node-focus (NF) transition point to move around without noticeable impact on the eigenvalues  $Re$ -trajectories, as can be concluded from figures 3(c,d) and 5(a). It becomes clear that for wavenumber slightly beyond  $\kappa \gtrsim 1.52$  the trajectories will experience an additional couple of zero-crossings, adding a pair of Hopf bifurcation points to the already existing one. This is illustrated for  $\kappa = 1.53$  in figure 10(a), where the successive crossings along the upper branch have been labelled  $H_1$ ,  $H_2$  and  $H_3$  as  $Re$  is increased. Continuation of the modulated waves branch for  $\kappa = 1.53$ , shown in figure 10(b), reveals that they connect supercritically to the upper branch of travelling waves in both directions at the two Hopf points that are at a larger distance from the saddle-node bifurcation, i.e.  $H_2$  and  $H_3$  of figure 10(a). The fold-of-cycles that was present at  $\kappa = 1.52$  is no longer present at  $\kappa = 1.53$ .

We shall extend this notation,  $H_1$ ,  $H_2$  and  $H_3$ , to denote the three potential Hopf crossings for any  $\kappa$  in the range studied. It is clear that for decreasing  $\kappa$ ,  $H_1$  and  $H_2$  approach, collide and disappear leaving  $H_3$  alone. Instead, for increasing  $\kappa$  it is  $H_2$  and  $H_3$  that approach and collide, leaving  $H_1$  alone as long as the node-focus point remains on the right side of the complex plane.

Adding the  $Re$ -dependence helps to clarify the situation. This is done in figure 11, where  $\varepsilon_{3D}$  has been plotted as a function of  $Re$  and  $\kappa$  (varying gray intensity as indicated by the legend) for both travelling waves (solid, dotted and dashed thick lines for 0, 1 and 2-dimensional unstable manifolds) and modulated waves (filled circles indicating minimum and maximum values of  $\varepsilon_{3D}$  along a period). Lower-branch travelling waves



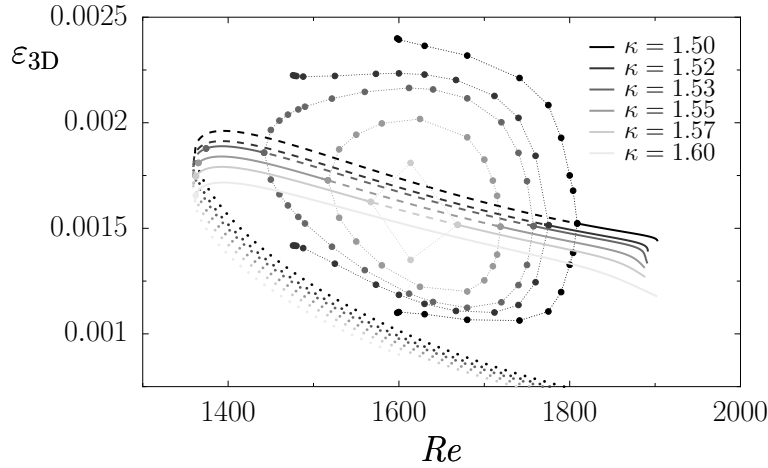


FIGURE 11. Non-axisymmetric streamwise-dependent energy ( $\varepsilon_{3D}$ ) as a function of  $Re$  and  $\kappa$  (different gray intensities as indicated in the legend). Lines represent travelling waves: solid, dotted and dashed for 0, 1 and 2 unstable directions. Filled circles on the curves represent Hopf points. The rest of circles represent stable modulated waves.

have a single unstable direction. For all cases shown, as they turn around the saddle-node point, a second unstable direction appears. Low- $\kappa$  (e.g.  $\kappa = 1.52$ ) waves remain unstable until they regain stability at Hopf bifurcations, whence supercritical branches of stable modulated waves are issued, as already discussed for figure 9. Traces of the turning point that we identified with a fold-of-cycles are clear from the bending tips of the modulated wave branches. High- $\kappa$  (e.g.  $\kappa = 1.60$ ) waves regain stability almost immediately at Hopf bifurcations but no stable branch of waves could be detected. Intermediate- $\kappa$  (e.g.  $\kappa = 1.53$ ) waves exhibit a mixed behaviour by regaining stability early on the upper branch, but losing it again temporarily for some range of  $Re$ . The whole intervening unstable range is nevertheless *covered* by a stable branch of modulated waves connecting both Hopf points, as illustrated in figure 10(b). At even higher  $\kappa$  (not shown), travelling waves become stable at the saddle-node, as was the case for  $\kappa = 1.70$  of figures 3(b,d). Returning to upper-branch travelling waves that were unstable at onset, the branch of modulated waves that must be born at their early stabilisation could not be detected with time evolution. This is a clear sign that they may bifurcate subcritically, with the branch pointing in the increasing  $Re$  direction.

Figure 12 shows the angular frequency  $\omega$  of the modulated waves as a function of  $Re$  and  $\kappa$ . Only a subset of  $\kappa$  has been plotted for clarity. And, of course, only as long as the branch is stable, i.e. accessible through time evolution. Along with the waves, the locus of Hopf bifurcation points (thin dotted line with crosses) has been added by plotting the imaginary part of the bifurcating eigenvalues. Along this curve,  $\kappa$  varies continuously but not monotonically. The curve has been split in three monotonical segments corresponding to the up to three independent zero-crossings that the complex pair of eigenvalues might undergo ( $H_1$ ,  $H_2$  and  $H_3$ ). Naturally, the modulational frequency of the bifurcating modulated waves is dictated by the imaginary part of the eigenvalues at the Hopf bifurcation. This figure strongly endorses the fold-of-cycles hypothesis for the non-reconnecting branches. The decreasing frequency around the fold-of-cycles is also suggestive of the eventual saddle-loop collision with lower-branch travelling waves, which demands a vanishing frequency (period going to infinity) as the modulated wave transforms into a non-robust homoclinic loop and disappears.

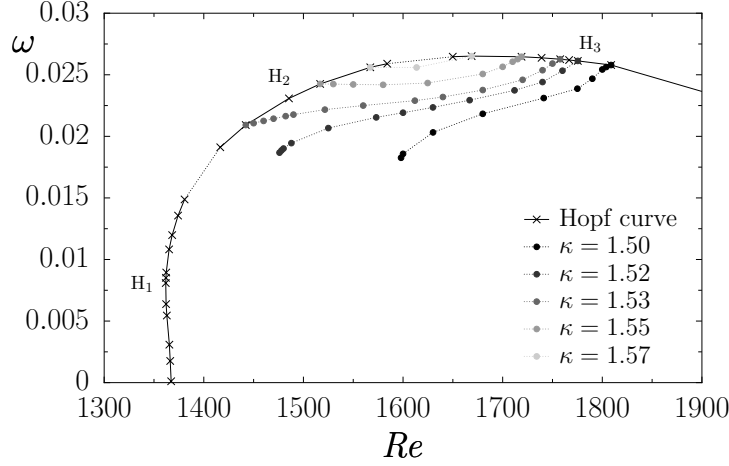


FIGURE 12. Angular frequency ( $\omega$ ) of the modulated waves and the Hopf points (filled circles). The thin line with crosses represents the imaginary part of the bifurcating eigenvalues along the locus of Hopf bifurcation points. The three segments, labelled  $H_1$ ,  $H_2$  and  $H_3$ , correspond to intersections of the Hopf curve with iso- $\kappa$  lines.

It is clear that for  $1.52 \lesssim \kappa \lesssim 1.53$  a change of behaviour takes place. Modulated wave branches go from reconnecting to the Hopf curve to bending and losing stability. It seems therefore reasonable that for some intermediate value, a branch of solutions may become tangent to the Hopf curve, precisely at the  $\kappa$  value for which the couple of additional eigenvalue crossings start occurring, i.e. where  $H_1$  and  $H_2$  merge. Slightly above this value, the curve would split in two. One of the segments connects supercritically two of the three existing Hopf points ( $H_2$  and  $H_3$ ). The other segment would be issued from the third Hopf point ( $H_1$ ) and, for purely geometrical reasons, it would have to do so supercritically towards lower  $Re$ . Unfortunately, the room left in parameter space for the stable branch of waves before it bends back and becomes unstable is tiny and very close to the Hopf bifurcation line where the relevant complex pair of eigenvalues exhibits a vanishing real part. As a consequence, transients are far too long to allow computation of the stable modulated waves in a feasible time-scale. This ultimately renders the numerical determination of the borders of existence of such solutions within this region extremely difficult. For even higher  $\kappa$ , but not exceeding the value for which upper-branch travelling waves are stable at onset, modulated waves can only bifurcate subcritically from  $H_1$  towards increasing  $Re$  and with vanishing frequencies, as required by the double-zero bifurcation scenario that takes place.

### 3.3. Unfolding of the Takens-Bogdanov bifurcation

The 2-fold azimuthally-periodic, shift-reflect symmetric family of travelling waves has been continued both in  $Re$  and  $\kappa$ , and systematic linear stability analysis has been carried out. In this manner, the locus of the saddle-node bifurcation between upper- and lower-branch travelling waves, and that of the Hopf bifurcation of upper-branch travelling waves has been tracked in parameter space. Results are summarised in figure 13. To the left of the saddle-node bifurcation lines ( $SN_+$  and  $SN_-$ ), there exist no travelling waves. These appear in saddle-node bifurcations to the right of the saddle-node lines. Upper-branch waves produced in  $SN_+$  are stable nodes, whereas those appearing in  $SN_-$  are unstable, all lower-branch travelling waves being unstable with a single unstable direction. Almost immediately after springing into existence, upper-branch travelling waves experience a

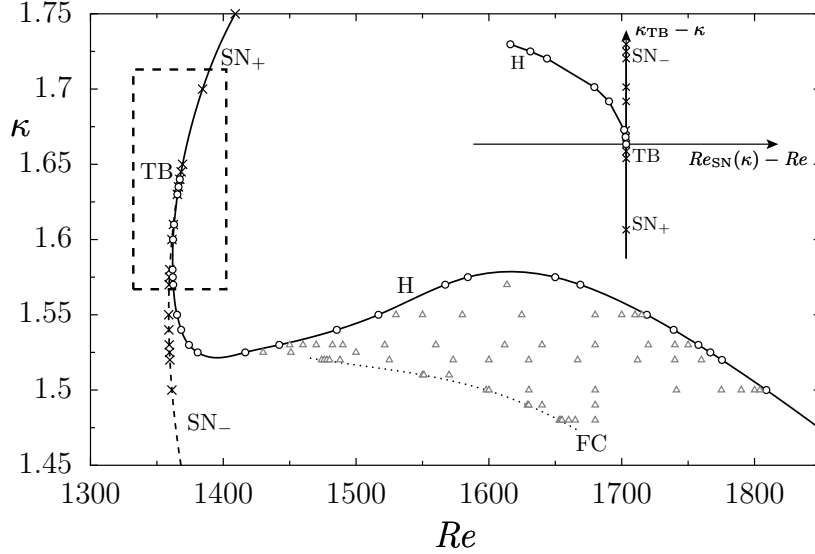


FIGURE 13. Bifurcation curves in  $(\kappa, Re)$ -parameter space.  $SN_+$  (solid line with crosses) and  $SN_-$  (dashed line with crosses) represent stable and unstable saddle-node bifurcations of travelling waves.  $H$  (solid line with circles) is the Hopf bifurcation curve of upper-branch travelling waves.  $TB$  is the Takens-Bogdanov (double-zero) bifurcation point. Stable modulated waves are indicated with triangles, with  $FC$  (dotted line) representing a fold-of-cycles. The inset shows a transformed zoom of the dashed region, with new coordinate axes  $\kappa_{TB} - \kappa$  and  $Re_{SN}(\kappa) - Re$ .

node-focus transition (NF of figure 3). This non-bifurcation curve is not shown in the figure, as it is extremely close to the saddle-node curve.  $SN_+$ ,  $SN_-$  and NF emanate from a Takens-Bogdanov or double-zero bifurcation point ( $TB$ ). At this point, two real eigenvalues collide exactly at the origin of the complex plane and become a conjugate pair. From this very same point, a Hopf bifurcation line ( $H$ ) is issued downwards to the right of  $SN_-$ . Initially, the lower is  $\kappa$ , the further away  $H$  gets from  $SN_-$ . This is a consequence of the left-opening parabolic shape of the complex eigenvalues (figure 3). As  $\kappa$  is reduced, NF moves away from the origin and the distance along the trajectory, which is related to  $Re$ , before crossing gets longer. Further along  $H$ , a couple of successive upward and downward bendings occur. The three segments into which they split the curve can be identified with  $H_1$ ,  $H_2$  and  $H_3$ , the three potential crossings the eigenvalues may undergo at any given  $\kappa$ . Above this line, upper-branch travelling waves are stable. Below it they are always unstable. As a consequence of its last downwards turn, for sufficiently large  $Re$  all upper-branch solutions are left stable as far as this bifurcation diagram is concerned and no secondary instabilities take place. To complete the phenomenological description, modulated waves have also been added into the picture (empty triangles). They occupy a region enclosed between the Hopf line and another line defined as the locus of turning points where modulated waves cease to exist. This line is a bifurcation curve corresponding to a fold-of-cycles ( $FC$ ), whereby stable modulated waves turn around and become unstable.

#### 4. Discussion

It is at this point convenient to define an alternative couple of parameters:  $\kappa_{TB} - \kappa$  and  $Re_{SN}(\kappa) - Re$ , where  $\kappa_{TB}$  is the value of  $\kappa$  at the Takens-Bogdanov point and  $Re_{SN}(\kappa)$  is the value of  $Re$  at the saddle-node point for each given  $\kappa$ . The transformation has been

applied to the region indicated by the dashed square in figure 13 and plotted in the inset. The resulting bifurcation diagram is reminiscent of the double-zero bifurcation described in Wiggins (2003). Of the two equivalent normal forms proposed for this bifurcation by Takens (1974) and Bogdanov (1975), the former can be applied to the present bifurcation by simply taking  $\mu_1 \simeq \kappa_{\text{TB}} - \kappa$  and  $\mu_2 \simeq \text{Re}_{\text{SN}}(\kappa) - \text{Re}$  in Wiggins (2003):

$$\begin{cases} \dot{x} = y, \\ \dot{y} = \mu_1 + \mu_2 y + x^2 + bxy, \end{cases} \quad (4.1)$$

with  $b = +1$ . A detailed analysis of the alternative normal form can be found in Kuznetsov (1995).

This second-order normal form provides an accurate description of all the phenomenology observed in the immediate vicinity of the Takens-Bogdanov point and gives additional information not accessible with the methodology here deployed. From the Takens-Bogdanov (TB) point (inset of figure 13), stable ( $\text{SN}_+$ ) and unstable ( $\text{SN}_-$ ) saddle-node lines extend along the vertical axis downwards and upwards, respectively. Issued from the same point is a subcritical Hopf curve (H) with a left-opening half-parabolic shape, to the left of the unstable saddle-node line. The unstable node created at the saddle-node immediately becomes a focus and later recovers stability upon crossing the Hopf curve leftwards. An unstable branch of unstable periodic orbits originates surrounding the stabilised equilibrium. Close analysis of the bifurcation reveals that the unstable periodic orbits grow large and collide with the unstable saddle in a saddle-loop homoclinic bifurcation, not shown in the figure. The unstable periodic orbits disappear with no consequence for the saddle equilibrium, leaving it, together with the stable focus, as the only surviving solutions. A saddle-loop curve, also branching off the Takens-Bogdanov point, must therefore be present, although it cannot be detected with the methods available.

Analysis of the second-order normal form is nevertheless insufficient to account for the existence of stable modulated waves and the back and forth bending of the Hopf curve. It is however possible to analyse in some detail what the effect of higher-order terms would be if the conditions for a non-degenerate double-zero bifurcation were nearly violated and higher-order terms were not negligible some distance away from the bifurcation point. A complete analysis of the codimension-3 bifurcation resulting from a vanishing second-order coefficient ( $b$  in 4.1) can be found in Dumortier *et al.* (1991). It is unlikely, unless some symmetry at play cancels exactly some second-order coefficients, which is not the case (the eigenfunctions involved preserve all symmetries of the solution), that simple tuning of two parameters will cross a codimension-3 point. Therefore, it is not the codimension-3 point we are interested in, but a perturbation around it that renders higher-order terms important at some distance from the codimension-2 point under analysis.

Such an analysis was carried out by Barkley (1990) when studying similar phenomena in plane Poiseuille flow, i.e. the appearance of modulated waves in channel flow. Previous studies (Pugh & Saffman 1988; Soibelman & Meiron 1991) had reported the onset of a modulational instability of travelling waves when the flow was driven by a constant pressure gradient. No instability was detected for the same waves when the flow was driven at constant mass-flux. Introducing a new parameter allowing to connect continuously both possible boundary conditions, a bifurcating scenario arose as a natural explanation. It was suggested that while a double-zero bifurcation could explain the appearance of unstable modulated waves, the simple inclusion of third-order terms to the second-order normal form could explain the existence of stable modulated waves for some parameter range. According to normal form theory, the extended normal form needs only include a couple of third-order terms (Guckenheimer & Holmes 1983; Knobloch 1986; Ioos &

Adelmeyer 1998)

$$\begin{cases} \dot{x} = y, \\ \dot{y} = \mu_1 + \mu_2 y + x^2 + k_1 x y + k_2 x^3 + k_3 x^2 y, \end{cases} \quad (4.2)$$

where appropriate scaling can be performed such that  $k_3 = \pm 1$ . The second order coefficient  $k_1$  is required to be sufficiently small so that third-order terms come into play, but non-zero so that non-degeneracy of the regular Takens-Bogdanov is preserved for sufficiently small  $\mu_1$  and  $\mu_2$ .

We shall not reproduce here the analysis of the third-order-extended normal form for the Takens-Bogdanov bifurcation. Instead, we refer the reader to Barkley (1990) for a detailed unfolding, and pick up on the main results that are relevant to the present case. It can be shown that appropriate tuning of the coefficients enables this normal form to capture some of the phenomenology observed but so far unexplained. Namely, setting  $k_3 = +1$  and  $k_1 > 0$ , gives the right eigenvalues path up to the first right turn after the node-focus transition (figures 3*c,d* and 5*a*). As a consequence, the Hopf curve experiences a first turning point as seen in figure 13, allowing for multiplicity of Hopf points at any given  $\kappa$  above some minimum value. A most relevant result concerns the nature of the Hopf curve itself. It has already been mentioned that in the vicinity of the Takens-Bogdanov point, the Hopf curve happens to be subcritical in the sense that the first Lyapunov coefficient is positive and bifurcating periodic orbits are unstable. Restricting (4.2) to the Hopf curve and with an appropriate change of variables and rescaling, we obtain

$$\begin{cases} \dot{\rho} = \rho(\beta_1 + \beta_2 \rho^2 + s\rho^4) + O(\rho^7), \\ \dot{\phi} = 1, \end{cases} \quad (4.3)$$

with  $s = +1$ , which is the normal form for the degenerate Hopf or Bautin bifurcation (Kuznetsov 1995).  $\beta_2 \sim k_1 - 3k_2\mu_2$  is the first Lyapunov coefficient and governs the change in criticality along the Hopf curve. Taking  $k_2 > 0$  will have  $\beta_2$  vanish for some value of  $\mu_2$ , leaving the Hopf curve supercritical beyond some point sufficiently far from the Takens-Bogdanov point. This is exactly what is needed to account for supercritical bifurcation of stable modulated waves. Careful analysis of the Bautin bifurcation also requires that the stable modulated waves turn around in a fold-of-cycles (FC), whenever they cannot branch to another Hopf point, becoming unstable. Since the original unstable waves collided with the saddle in a saddle-loop bifurcation in the frame of the Takens-Bogdanov bifurcation, it is to be expected that they will continue exhibiting the same behaviour even if they now initially bifurcate supercritically. Thus, even though we could only follow stable modulated waves to their fold bifurcation (figure 11), we can now reliably comment on their fate: they should most certainly disappear in saddle-loop bifurcations. This was already justified upon explaining figure 12, where the trend of the angular frequency suggested that the period could go to infinity after turning around, as the saddle-loop bifurcation requires for the homoclinic connection in which they convert before disappearing. The Bautin point must be somewhere along the Hopf curve before the first turning point. As it happens, supercriticality is only extremely mild until about the turning point (the locus of the fold-of-cycles appears to be very close to the Hopf curve), resulting in our inability to compute the stable modulated waves that must be present. This is so because close to the Hopf curve, the dynamics are extremely slow and the transients accordingly long. These are the waves that are expected to turn around, become unstable and are destroyed in saddle-loops as predicted by third-order terms. Beyond the turning point, supercriticality means branching towards lower  $\mu_1$  (higher

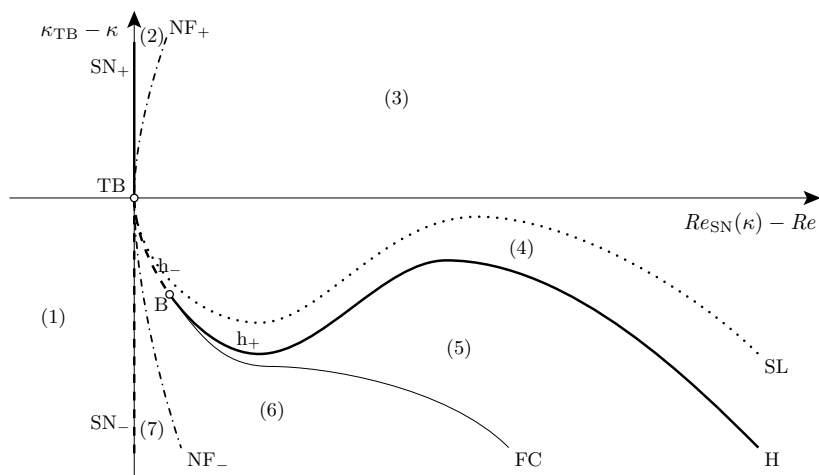


FIGURE 14. Attemptive bifurcation diagram in  $(\kappa_{TB} - \kappa, Re_{SN}(\kappa) - Re)$ -parameter space. Represented are the two codimension-2 points TB (double zero or Takens-Bogdanov) and B (Bautin or degenerate Hopf). B splits the Hopf curve (H) in two segments, one subcritical ( $h_-$ , dashed thick line), the other supercritical ( $h_+$ , solid thick line). From TB, stable and unstable saddle-node curves ( $SN_+$  and  $SN_-$ ), the Hopf curve and a saddle-loop curve (SL, dotted line) are born, together with stable and unstable node-focus transition curves ( $NF_+$  and  $NF_-$ , dash-dotted lines). A fold of cycles (FC) is issued from B. Numbers in parenthesis indicate different regions.

$Re$ ). These waves we have computed, but their fate crucially depends upon the second turning of the Hopf curve, and third-order terms tell us nothing about it.

Adding fourth-order terms is a straightforward but tedious calculation that we shall not reproduce here. It cannot be expected that fourth-order amplitude equations capture the behaviour reliably so far from the Takens-Bogdanov point, yet there is strong numerical evidence that fourth-order terms have a say. They allow for an extra turning point to the Hopf curve, without altering any of the previous predictions. As a result, stable modulated waves born between the two turning points can disappear in a second supercritical Hopf after the second turn, as illustrated in figures 11 and 13. Further down the Hopf curve, beyond the second turning point, stable modulated waves either behave as just explained or progress stably until they meet the fold-of-cycles (FC) and turn around. This curve must emerge from the Hopf curve precisely at the Bautin point, the existence of which can be inferred but its location not determined precisely with the tools at hand.

Figure 14 completes the picture just sketched in an endeavouring diagram for all bifurcations in parameter space. Modified parameters  $(\kappa_{TB} - \kappa, Re_{SN}(\kappa) - Re)$  have been chosen for simplicity. The full diagram is organised around the Takens-Bogdanov (TB) codimension-2 point. This point separates two branches of saddle-node lines ( $SN_+$  and  $SN_-$ ). At  $SN_+$  a stable node and a saddle equilibrium coalesce, while crossing  $SN_-$  generates an unstable node and a saddle. The node, stable or unstable, experiences a quick transition and becomes a focus, stable or unstable, in a node-focus transition ( $NF_+$  and  $NF_-$ ). These are non-bifurcation curves. From TB, a Hopf bifurcation curve H springs quadratically to the same side as  $SN_-$ . Sufficiently close to TB periodic orbits bifurcate subcritically from the node at H ( $h_-$ ). Further away, H changes criticality at a codimension-2 Bautin point (B, degenerate Hopf) and becomes supercritical ( $h_+$ ). At B, a fold-of-cycles curve (FC) is born to the  $h_+$  side of H and parting from it quadratically. Between  $h_+$  and FC, stable periodic orbits exist. At  $h_-$  and FC, unstable periodic orbits are generated. They must all cease to exist, at least in the vicinity of TB, in saddle-loop

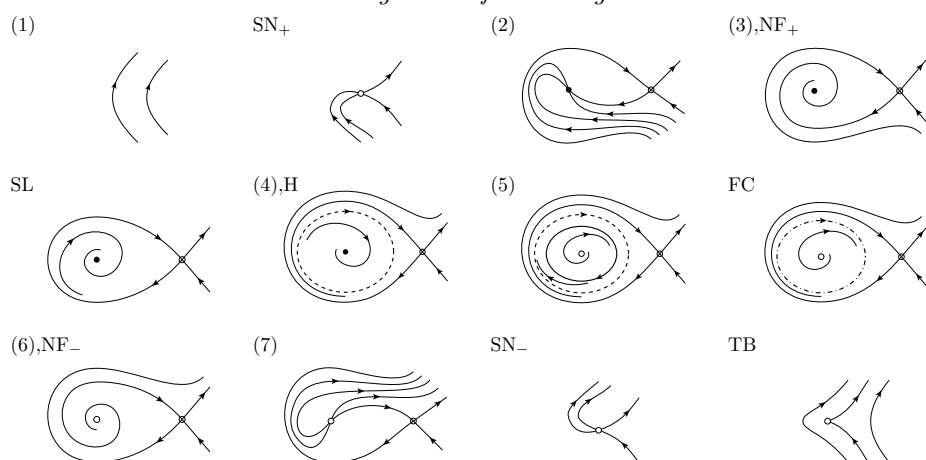


FIGURE 15. Phase map diagrams corresponding to all bifurcation curves and numbered regions in figure 14. Small circles correspond to relative equilibria (filled for stable equilibria), and closed thick lines to relative periodic orbits (solid for stable, dashed for unstable orbits). Thin lines with arrows indicate stable and unstable manifolds, homoclinic and heteroclinic connections.

bifurcations (SL). At SL, the unstable periodic orbit has grown large and collides with the saddle producing a non-robust homoclinic cycle. The periodic orbit vanishes while the saddle experiences no change whatsoever. Among all bifurcation curves drawn in figure 14, SL is the most uncertain. Since it runs on the saddle, independent from the nodal equilibrium, there is no restriction on whether this line can cross  $H$ . Thorough analysis of the Takens-Bogdanov bifurcation shows that it cannot cross  $h_-$  and that it actually departs quadratically from  $SN_-$ , but higher-order terms can easily make it cross  $h_+$ . Unfortunately no linear stability analysis of the saddle can cast light on the issue, nor can the unstable periodic orbits be tracked with time evolution. However, the picture just sketched would not change much.

Figure 15 shows phase map diagrams of the flow projected on the 2-dimensional centre manifold. The labels indicate to which region in figure 14 each phase map corresponds. Making a clockwise round-trip can help clarify the picture. Starting from (1), where no solutions exist, and crossing  $SN_+$  into (2) a saddle and a stable node are created. The stable node turns into a stable focus through  $NF_+$  in (3). In (4), an unstable periodic orbit exists, that has been created in SL. Upon crossing  $h_+$  into (5) a stable cycle appears around the focus, which becomes unstable. The coexistence of an unstable and a stable cycle in (5) lasts until they collide and disappear in FC, leaving only the saddle and an unstable focus in (6). It is possible to arrive to (6) directly from (4). In this case, the unstable cycle just merges with the stable focus in  $h_-$  to leave an unstable focus. Crossing  $NF_-$  the unstable focus transforms into an unstable node in (7). The unstable focus coalesces with the saddle through  $SN_-$  back into region (1). The possible crossing of SL and  $h_+$  would only affect the order in which the stable cycle merges with the focus and the unstable cycle collides with the saddle, when going from (5) to (3).

It is at this point necessary to justify why we have not made use of the discrete azimuthal periodicity or of the shift-reflect symmetry in deriving the normal form. The fact is that we are entitled to ignore these symmetries because they play no significant role in the problem at hand. If any of the solutions had broken any of the symmetries, these would have needed to be built into the normal form. Since there is no numerical evidence from either time evolution or linear stability that this happens, these symmetries can be safely ignored.

## 5. Conclusion

A complex bifurcating scenario in pipe Poiseuille flow, involving the appearance of travelling as well as modulated travelling waves, has been thoroughly analysed within a given azimuthal subspace, taking advantage of the special stability properties of the solutions it is home to. These stability properties make this subspace particularly fit for the search and analysis of all kinds of exotic behaviour including, but not limited to, the double-zero bifurcation here unfolded. This can help place a lower bound to the extreme complexity that must certainly be present in full space pipe flow.

The particular family of waves studied involves the appearance in Hopf bifurcations of modulated waves that are either unstable at onset or become unstable in a fold-of-cycles. It cannot be guaranteed that the unstable modulated waves created in the fold-of-cycles eventually disappear in a saddle-loop bifurcation. Their ultimate fate depends on the absence of symmetry-breaking bifurcations that free them from the need of colliding with the saddle or that allow for an entanglement of the stable and unstable manifolds of the saddle in the vicinity of the global bifurcation. While such a behaviour has to be expected generically, the absence of chaotic dynamics around the saddle suggests that this is not the case, and that the scenario described may be fairly accurate.

The Takens-Bogdanov bifurcation experienced by this particular family of travelling waves must not be considered as an exotic scenario. There is strong evidence that other families of travelling waves might be bifurcating in similar environments. This is the case of the highly-symmetric 3-fold azimuthally-periodic family of travelling waves described in Pringle *et al.* (2009), for which the eigenvalue associated with the saddle-node bifurcation is known to collide with another eigenvalue and go complex immediately after crossing from lower to upper branch. This happens in the context of instability dictated by several additional unstable eigenvalues, which renders the techniques used in the present study unable to unfold the bifurcation. Nevertheless, a Takens-Bogdanov bifurcation appears to be there all the same.

The scenario is nonetheless not general. Other families of travelling waves, such as the mirror-symmetric 2-fold azimuthally-periodic, do not follow this behaviour. Other travelling waves come from Pitchfork bifurcations from other more symmetric waves, e.g. the shift-reflect azimuthally non-periodic travelling wave (Pringle & Kerswell 2007), which comes from symmetry breaking of a mirror-symmetric wave. The Takens-Bogdanov bifurcation simply does not apply in these cases.

As a result of a Takens-Bogdanov bifurcation, no trace of modulated waves is expected to survive long enough to take part in the formation of a chaotic attractor or saddle as a precursor to turbulent dynamics. Nevertheless, it is interesting to point out that, far enough from the Takens-Bogdanov point, only stable upper-branch solutions are left. Thus, all the techniques here deployed are left valid for an eventual analysis of the bifurcation cascade they may undergo at higher  $Re$ . A detailed study of the behaviour of these waves at higher flow rates is currently underway.

This work has been supported by the Spanish Ministry of Science and Technology, under grants FIS2007-61585, by the Catalan Government under grant SGR-00024, and by the Deutsche Forschungsgemeinschaft.

## REFERENCES

- BARKLEY, D. 1990 Theory and predictions for finite-amplitude waves in 2-dimensional plane Poiseuille flow. *Phys. Fluids A* **2** (6), 955–970.



- BOBERG, L. & BROSIA, U. 1988 Onset of turbulence in a pipe. *Z. Naturforsch. A: Phys. Sci.* **43**, 697–726.
- BOGDANOV, R. 1975 Versal deformations of a singular point on the plane in the case of zero eigenvalues. *Func. Anal. Appl.* **9** (144–145).
- BROSIA, U. & GROSSMANN, S. 1999 Minimum description of the onset of pipe turbulence. *Eur. Phys. J. B* **9** (2), 343–354.
- CHOSSAT, P. & LAUTERBACH, R. 2000 *Methods in Equivariant Bifurcations and Dynamical Systems*. London: World Scientific Publishing.
- DARBYSHIRE, A.G. & MULLIN, T. 1995 Transition to turbulence in constant-mass-flux pipe flow. *J. Fluid Mech.* **289**, 83–114.
- DENNIS, J.E. & SCHNABEL, R.B. 1996 *Numerical Methods for Unconstrained Optimization and Nonlinear Equations*. Englewood Cliffs, N.J.: SIAM.
- DUGUET, Y., WILLIS, A.P. & KERSWELL, R.R. 2008 Transition in pipe flow: the saddle structure on the boundary of turbulence. *J. Fluid Mech.* **613**, 255–274.
- DUMORTIER, F., ROUSSARIE, R., SOTOMAYOR, J. & ZOLADEK, H. 1991 *Bifurcations of Planar Vector Fields. Nilpotent Singularities and Abelian Integrals*. Berlin: Springer-Verlag.
- ECKHARDT, B. 2009 Introduction. Turbulence transition in pipe flow: 125th anniversary of the publication of Reynolds' paper. *Phil. Trans. Roy. Soc. Lond. A* **367** (1888), 449–455.
- ECKHARDT, B., SCHNEIDER, T.M., HOF, B. & WESTERWEEL, J. 2007 Turbulence transition in pipe flow. *Ann. Rev. Fluid Mech.* **39**, 447–468.
- EHRENSTEIN, U. & KOCH, W. 1991 3-dimensional wave-like equilibrium states in plane Poiseuille flow. *J. Fluid Mech.* **228**, 111–148.
- FAISST, H. & ECKHARDT, B. 2003 Travelling waves in pipe flow. *Phys. Rev. Lett.* **91** (22), 224502.
- FRAYSSÉ, V., GIRAUD, L., GRATTON, S. & LANGOU, J. 2003 A set of gmres routines for real and complex arithmetics on high performance computers. Technical Report TR/PA/03/3. CERFACS, <http://www.cerfacs/algos/Softs>.
- FREITAG, M. A. 2007 Inner-outer iterative methods for eigenvalue problems - convergence and preconditioning. PhD thesis, University of Bath, Bath, U.K.
- GOLUBITSKY, M., LEBLANC, V.G. & MELBOURNE, I. 2000 Hopf bifurcation from rotating waves and patterns in physical space. *J. Nonlinear Sci.* **10** (1), 69–101.
- GROSSMANN, S. 2000 The onset of shear flow turbulence. *Rev. Modern Phys.* **72** (2), 603–618.
- GUCKENHEIMER, J. & HOLMES, P. 1983 *Nonlinear Oscillations, Dynamical Systems, and Bifurcations of Vector Fields*. New York: Springer-Verlag.
- HOF, B., VAN DOORNE, C.W.H., WESTERWEEL, J., NIEUWSTADT, F.T.M., FAISST, H., ECKHARDT, B., WEDIN, H., KERSWELL, R.R. & WALEFFE, F. 2004 Experimental observation of nonlinear travelling waves in turbulent pipe flow. *Science* **305** (5690), 1594–1598.
- HOF, B., SCHNEIDER, T.M., WESTERWEEL, J. & ECKHARDT, B. 2006 Finite lifetime of turbulence in shear flows. *NATURE* **443** (7107), 59–62.
- IOOS, G. & ADELMAYER, M. 1998 *Topics in Bifurcation Theory and Applications*, 2nd edn. London: World Scientific Publishing.
- KERSWELL, R.R. & TUTTY, O.R. 2007 Recurrence of travelling waves in transitional pipe flow. *J. Fluid Mech.* **584**, 69–102.
- KNOBLOCH, E. 1986 Normal forms for bifurcations at a double zero eigenvalue. *Phys. Lett. A* **115** (5), 199–201.
- KRUPA, M. 1990 Bifurcations of relative equilibria. *SIAM J. Math. Anal.* **21** (6), 1453–1486.
- KUZNETSOV, Y.A. 1995 *Elements of Applied Bifurcation Theory*, 3rd edn. New York: Springer-Verlag.
- LEHOUCQ, R. & SCOTT, J. A. 1996 An evaluation of software for computing eigenvalues of sparse nonsymmetric matrices. Technical Report MCS-P547-1195. Argonne National Laboratory, <http://www.caam.rice.edu/software/ARPACK>.
- MAMUN, C.K. & TUCKERMAN, L.S. 1995 Asymmetry and Hopf bifurcation in spherical Couette flow. *Phys. Fluids* **7** (1), 80–91.
- MELLIBOVSKY, F. & MESEGUER, A. 2009 Critical threshold in pipe flow transition. *Phil. Trans. Roy. Soc. Lond. A* **367** (1888), 545–560.
- MESEGUER, A., AVILA, M., MELLIBOVSKY, F. & MARQUES, P. 2007 Solenoidal spectral formu-

- lations for the computation of secondary flows in cylindrical and annular geometries. *Eur. Phys. J. Special Topics* **146**, 249–259.
- MESEGUER, A. & MELLIBOVSKY, F. 2007 On a solenoidal Fourier-Chebyshev spectral method for stability analysis of the Hagen-Poiseuille flow. *Appl. Num. Math.* **57**, 920–938.
- MESEGUER, A. & TREFETHEN, L.N. 2003 Linearized pipe flow to Reynolds number  $10^7$ . *J. Comput. Phys.* **186**, 178–197.
- NAGATA, M. 1997 Three-dimensional traveling-wave solutions in plane Couette flow. *Phys. Rev. E* **55** (2), 2023–2025.
- PFENNIGER, W. 1961 *Boundary Layer and Flow Control*, chap. Transition in the inlet length of tubes at high Reynolds numbers, pp. 970–980. Pergamon.
- PRINGLE, C.C.T., DUGUET, Y. & KERSWELL, R.R. 2009 Highly symmetric travelling waves in pipe flow. *Phil. Trans. Roy. Soc. Lond. A* **367** (1888), 457–472.
- PRINGLE, C.C.T. & KERSWELL, R.R. 2007 Asymmetric, helical, and mirror-symmetric traveling waves in pipe flow. *Phys. Rev. Lett.* **99** (7), 074502.
- PUGH, J.D. & SAFFMAN, P.G. 1988 Two-dimensional superharmonic stability of finite-amplitude waves in plane poiseuille flow. *J. Fluid Mech.* **194**, 295–307.
- QUARTERONI, A., SACCO, R. & SALERI, F. 2007 *Numerical Mathematics*, 2nd edn. Berlin: Springer-Verlag.
- RAND, D. 1982 Dynamics and symmetry - Predictions for modulated waves in rotating fluids. *Arch. Ration. Mech. An.* **79** (1), 1–37.
- REYNOLDS, O. 1883 An experimental investigation of the circumstances which determine whether the motion of water shall be direct or sinuous and of the law of resistance in parallel channels. *Phil. Trans. Roy. Soc. Lond.* **174**, 935–982.
- SANCHEZ, J., MARQUES, F. & LOPEZ, J.M. 2002 A continuation and bifurcation technique for Navier-Stokes flows. *J. Comput. Phys.* **180** (1), 78–98.
- SCHMID, P.J. & HENNINGSON, D.S. 1994 Optimal energy growth in Hagen-Poiseuille flow. *J. Fluid Mech.* **277**, 197–225.
- SCHNEIDER, T.M., ECKHARDT, B. & VOLLMER, J. 2007 Statistical analysis of coherent structures in transitional pipe flow. *Phys. Rev. E* **75** (6), 066313.
- SCHNEIDER, T.M., ECKHARDT, B. & YORKE, J.A. 2007 Turbulence transition and edge of chaos in pipe flow. *Phys. Rev. Lett.* **99** (3), 034502.
- SHAN, H., MA, B., ZHANG, Z. & NIEUWSTADT, F.T.M. 1999 On the spatial evolution of a wall-imposed periodic disturbance in pipe Poiseuille flow at  $Re = 3000$ . Part 1. Subcritical disturbance. *J. Fluid Mech.* **398**, 181–224.
- SKUFCA, J.D., YORKE, J.A. & ECKHARDT, B. 2006 Edge of chaos in a parallel shear flow. *Phys. Rev. Lett.* **96** (17), 174101.
- SMALE, S. 1967 Differentiable dynamical systems .I. Diffeomorphisms. *Bull. Amer. Math. Soc.* **73** (6), 747–817.
- SOBELMAN, I. & MEIRON, D.I. 1991 Finite-amplitude bifurcations in plane Poiseuille flow - 2-dimensional Hopf-bifurcation. *J. Fluid Mech.* **229**, 389–416.
- TAKENS, F. 1974 Singularities of vector fields. *Publ. Math. IHES* **43** (47–100).
- WALEFFE, F. 1995 Hydrodynamic stability and turbulence - Beyond transients to a self-sustaining process. *Stud. Appl. Math.* **95** (3), 319–343.
- WALEFFE, F. 1997 On a self-sustaining process in shear flows. *Phys. Fluids* **9** (4), 883–900.
- WANG, J., GIBSON, J. & WALEFFE, F. 2007 Lower branch coherent states in shear flows: Transition and control. *Phys. Rev. Lett.* **98** (20), 204501.
- WEDIN, H. & KERSWELL, R.R. 2004 Exact coherent structures in pipe flow: travelling wave solutions. *J. Fluid Mech.* **508**, 333–371.
- WIGGINS, S. 2003 *Introduction to Applied Nonlinear Dynamical Systems and Chaos*, 2nd edn. New York: Springer-Verlag.
- WILLIS, A.P. & KERSWELL, R.R. 2008 Coherent structures in localized and global pipe turbulence. *Phys. Rev. Lett.* **100** (12).
- WYGNANSKI, I.J. & CHAMPAGNE, F.H. 1973 On transition in a pipe. Part 1. The origin of puffs and slugs and the flow in a turbulent slug. *J. Fluid Mech.* **59**, 281–335.
- WYGNANSKI, I.J., SOKOLOV, M. & FRIEDMAN, D. 1975 On transition in a pipe. Part 2. The equilibrium puff. *J. Fluid Mech.* **69**, 283–304.
- ZIKANOV, O.Y. 1996 On the instability of pipe Poiseuille flow. *Phys. Fluids* **8** (11), 2923–2932.